Reducing Shock Interactions in Transonic Turbine via Three-Dimensional Aerodynamic Shaping

Braden J. Hancock*
Brigham Young University, Provo, Utah 84604
and
John P. Clark†
U.S. Air Force Research Laboratory, Wright–Patterson Air Force Base, Ohio 45433

DOI: 10.2514/1.B35027

In a high-pressure turbine that is used in combination with a contrarotating low-pressure turbine, the geometry of the low-pressure turbine guide vane gives rise to a shock reflection that has a significant impact on the upstream blade. In consequence, both the performance of the high-pressure turbine and its resistance to high-cycle fatigue failure (i.e., its durability) can be affected. Here, a series of design studies is undertaken in an attempt to mitigate the unsteadiness that arises due to shock interactions in such a turbine. A new method for estimating the forcing function experienced by the high-pressure turbine blade is proposed and evaluated. This method, identified as approximation by surface normal projections, requires only the airfoil geometries and locations as input and demonstrates a significant advantage over an approach to three-dimensional aerodesign consisting exclusively of time-resolved, multirow simulations. The implementation of the approximation by surface normal projections method, in conjunction with a genetic algorithm, is shown to have resulted in superior airfoil geometries with respect to preventing high-cycle fatigue failure and with a reduction of computation time for the analysis of a single airfoil by four orders of magnitude.

Downloaded by MASSACHUSETTS INST OF TECHNOLOGY (MIT - LINCOLN LAB) on July 9, 2014 | http://arc.aiaa.org | DOI: 10.2514/1.B35027

Nomenclature

C_r	=	center of reflection (% span of airfoil)
$\boldsymbol{d}$	=	displacement vector
e	=	engine order, frequency/(rpm/60)
f	=	fitness
i	=	identifier of vertex on grid defining blade
k	=	rank of individual
m	=	magnitude of shock reflection
$\boldsymbol{n}$	=	surface normal vector
P_k	=	selective probability
r	=	radial distance of vertex from blade root
s	=	selective pressure
$\boldsymbol{x}$	=	Cartesian coordinate system location vector
$\boldsymbol{y}$	=	Cartesian coordinate system location vector
$\boldsymbol{z}$	=	Cartesian coordinate system location vector
μ	=	population size

I. Introduction

OVER the years, a large number of studies has been dedicated to increasing our understanding of the periodic unsteadiness inherent to flows in gas turbine engines. For example, the works of Tyler and Sofrin [1] and Rangwalla and Rai [2] consider the theoretical aspects of unsteady flows in turbomachines, whereas Dring et al. [3] and Dunn and Haldeman [4] focused on experiments at conditions relevant to operating engines, and Rai [5] and Giles [6] pioneered the simulation of flows dominated by rotor–stator interactions. Excellent introductions to the subject (e.g., Paniagua and Denos [7]) are available as well as comprehensive reviews of the state of the art (e.g., Greitzer et al. [8] and Sharma et al. [9]). Greitzer et al. [8] pointed out that, in general, levels of unsteady forcing that induce high-cycle fatigue (HCF) problems during engine development are not always well predicted. The authors concluded that blade forced-response and the high-cycle fatigue failures that can result from it are of sufficient interest to the gas-turbine community that "... a decrease in the level of empiricism [in that area] would be of significant value in the engine development process." Accordingly, many companies now include calculations of resonant stresses in multirow turbomachinery in their design processes [10–16].

When a high expansion ratio high-pressure turbine (HPT) is used in combination with a contrarotating low-pressure turbine (LPT), significant unsteadiness is generated when the inlet guide vane of the LPT induces a reflection of the incident shock wave from the HPT blade that propagates back upstream to impact the blade row that generated it. Large levels of unsteady forcing can then give rise to resonant stresses, and these can in turn induce HCF failure, as noted previously. To obviate HCF failures from these interactions, the number of downstream low-pressure turbine vanes is often increased to a level sufficient to ensure that no resonance occurs in the upstream blade row over the entire operating range of the engine. This is an example of what Greitzer et al. [8] dubbed resonant avoidance in turbine design. While it is effective in eliminating HCF failures, the increase in airfoil count in turn increases both engine weight and life-cycle costs, partially negating the benefits of contrarotation for the machine. Accordingly, it is prudent to assess whether it is possible to control shock interactions in a relevant turbine via fluid dynamic means.

To illustrate the topology of the unsteady interactions that occur in a contrarotating multispool turbomachine, an instantaneous distribution of both static density and entropy from a three-dimensional (3D) unsteady Reynolds-averaged Navier–Stokes (RANS) calculation of the U.S. Air Force Research Laboratory (AFRL) High-Impact Technologies Research Turbine (HITRT) is shown in Fig. 1. Note that the HPT blade row rotates, while the LPT vane row is stationary. The HPT blade is transonic with a design isentropic exit Mach number of 1.3. Static density ranges from 0.8 (blue) to 2.8 (red) kg/m^3. The flow through the blade row passes through a cross-channel shock wave that interacts with the suction-side boundary layer and reflects. This shock wave oscillates in position (see location 1 in Fig. 1). Additionally, an oblique shock emanates from the trailing edge of the

Presented as Paper 2013-0126 at the 51st AIAA Aerospace Sciences Meeting Including the New Horizons Forum and Aerospace Exposition, Grapevine, TX, 7–10 January 2013; received 28 April 2013; revision received 29 March 2014; accepted for publication 5 April 2014; published online 30 June 2014. This material is declared a work of the U.S. Government and is not subject to copyright protection in the United States. Copies of this paper may be made for personal or internal use, on condition that the copier pay the $10.00 per-copy fee to the Copyright Clearance Center, Inc., 222 Rosewood Drive, Danvers, MA 01923; include the code 1533-3876/14 and $10.00 in correspondence with the CCC.

*Research Assistant, Department of Mechanical Engineering; braden.hancock@byu.edu.

†Principal Engineer, Turbomachinery Branch, Turbine Engine Division, Aerospace Systems Directorate; john.clark3@wpafb.af.mil.

Downloaded by MASSACHUSETTS INST OF TECHNOLOGY (MIT - LINCOLN LAB) on July 9, 2014 | http://arc.aiaa.org | DOI: 10.2514/1.B35027

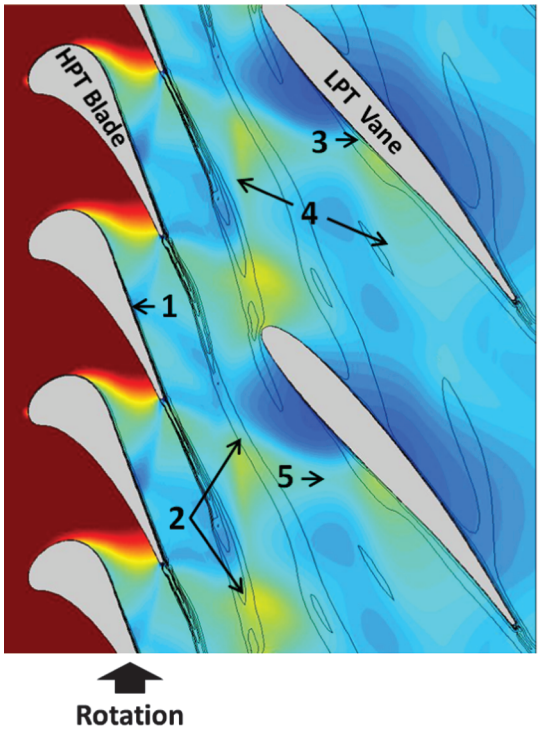

Fig. 1 Instantaneous distribution of static entropy and density in a contrarotating turbine.

suction side of the blade and proceeds downstream. As it does so, it interacts with the shear layer from the adjacent blade row (location 2) and ultimately impacts the boundary layer on the pressure side of the downstream vane. Since the blade is rotating, the position of this shock–boundary layer interaction sweeps upstream with time (location 3). The shock reflects from the vane pressure side, and this reflection also moves upstream as the blade rotates (location 4), ultimately becoming a pressure perturbation that propagates upstream to influence the time-resolved pressure and heat transfer on the suction side of the blade. Along the way, the reflected shock also crosses shear layers and shocks from the upstream blades (location 5). Collectively, the unsteady interactions are exceptionally complex, so it is prudent to base any attempt to mitigate the forcing function experienced by the HPT blade due to interactions with the downstream row on the basic physics of unsteady shock motion [17].

II. Manipulation of Airfoils for Control of Shock Interactions

It is well known that a moving shock wave like that extending downstream from the rotating blade of the HITRT induces a small velocity component normal to the shock and near coincident with its direction of travel. The moving shock wave must reflect from any stationary solid boundaries it impacts in order to maintain the no-slip condition at the surface. Furthermore, the portion of the induced motion that must be cancelled is the vector component normal to the surface of the boundary. So, it stands to reason that if the local normal vector of the surface is altered then the direction of travel of the reflected shock must also change. One can imagine a situation in which the 3D geometry of the downstream vane is altered in such a way that the shock reflections from it are directed at a region of the upstream blade that is less likely to experience high resonant stresses.

In the initial design of the HITRT downstream vane, the only three dimensionality that was included was a consequence of the local variation in inlet and exit air angles that were specified as a result of design iterations at the mean-line level. The vane was specified in three dimensions by stacking two-dimensional (2D) profiles on the centroids of the area of each section, and the geometry of the airfoil that resulted is shown in the center of Fig. 2. As an illustration of the

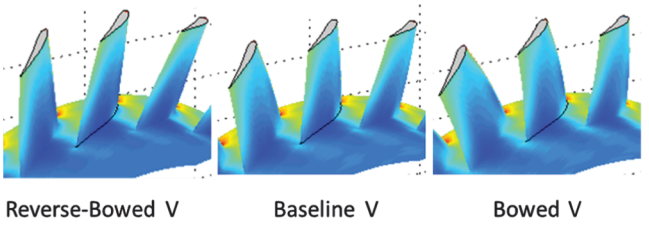

Fig. 2 Two bowed airfoils and the baseline airfoil for investigating 3D shaping effects.

effects of 3D shaping on vane–blade interaction, a pair of additional vanes was generated. For these airfoils, the 2D profiles at each radius specifying the HITRT vane were not altered. Instead, the location of the centroid of each 2D section of the airfoil was allowed to shift by an increasing percentage of the local pitch in either the positive or negative circumferential direction. The airfoils that resulted were called the bowed and reverse-bowed airfoils, and these vanes are shown on the left and right sides of Fig. 2, respectively.

The effect of 3D aerodynamic shaping of the downstream vane on the unsteady pressure experienced by the blade on the suction side is presented in Fig. 3a along with the baseline levels of the HITRT, shown in the center of the figure. Upstream of the location where the cross-channel shock impinges on the airfoil (i.e., location 1 of Fig. 1), the unsteadiness over the blade suction side is independent of the shape of the downstream airfoil. However, the effect of vane bow on the distribution of unsteadiness downstream of that location is profound. Reverse bowing tends to drive the unsteady pressure at the first harmonic of vane passing (46E) toward the blade tip, while bowing focuses it near the hub. Independent of the mode shape, there is far less airfoil motion near the blade root than the tip. Consequently, driving the unsteady pressures toward the hub is a benefit when one considers resonant stresses. Also, 3D shaping of the vane alters the distribution of phase angles over the blade suction side downstream of the cross-channel shock. Figure 3b is a plot of the variation in the phase angle with a span at approximately 95% axial chord due to the baseline vane as well as the bowed and reverse-bowed airfoils. One can see that the variation in the phase angle with span is greater with 3D shaping than for the baseline vane. Resonance requires that unsteady pressures at a given frequency are coincident with a mode shape. It also requires that the phase of the unsteadiness is consistent with the oscillation of the airfoil. One expects, then, that a greater variation in phase angle over the region of the blade impacted by shock reflections could also be beneficial from the standpoint of resonant stresses. This is not guaranteed to be true, since the net benefit or detriment achieved due to a variation in phase would depend on the mode shape(s) of interest. Still, a demonstrated capability to affect the phase of unsteadiness via airfoil shaping is of interest to the designer that might one day be faced with a need to manipulate that quantity to avoid or mitigate a resonant stress.

There are many examples in the literature of the 3D shaping of airfoils, although often the goal of such designs is to achieve a benefit in aeroperformance. One exception is the design-optimization study of Joly et al. [18,19] in which the geometric parameterization of the upstream vane was consistent with both the bow and lean of the airfoil. The authors sought to reduce the circumferential distortion in static pressure exiting the vane row in an effort to decrease the unsteadiness on the blade after Clark et al. [20]. However, unlike in the current study in which a modification of shock reflections is sought, the work of Joly et al. was more consistent with a reduction in the strength of incident shocks in the HITRT.

III. Optimization Using 3D Unsteady RANS Analysis

It is clear from the previous observations that it is possible to alter the variation in unsteady pressures on the upstream blade by bowing the downstream airfoil. It is also apparent that many embodiments of the airfoil bow can increase resonant stresses. Fortunately for the airfoil designer, improvements in gas-turbine computational fluid dynamics (CFD) have allowed for ever more sophisticated flowfield

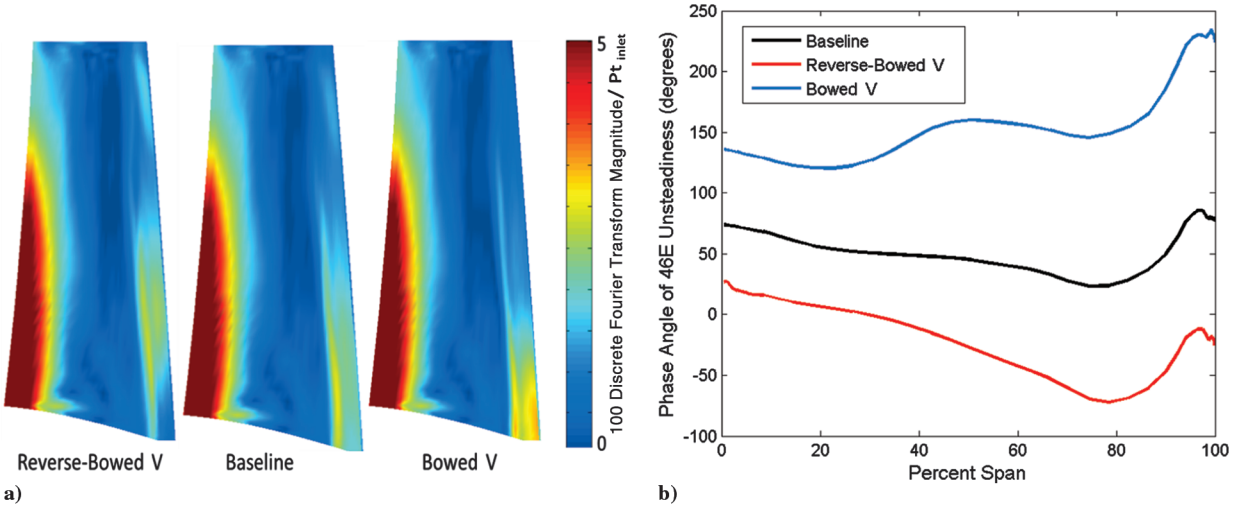

Fig. 3 The effect of 3D aerodynamic shaping on a) unsteadiness and b) phase angle variation.

predictions (e.g., Dunn [21] and Adamczyk [22]), and it is now possible to predict both the time-averaged and time-resolved pressure loadings on transonic airfoils with good accuracy within constraints consistent with appropriate code validation (e.g., Rao et al. [23], Busby et al. [24], Hilditch et al. [25], and many others [26–29]). Design-optimization systems have previously been used in conjunction with steady-state flow solvers with beneficial effects on transonic turbine airfoils (e.g., Jennions and Adamczyk [30] and Clark et al. [20]). Further development of predictive methods such as multigrid techniques and implicit dual time stepping, coupled with the parallelization of codes [31] have created the possibility for using 3D, unsteady Navier–Stokes analyses throughout the design cycle and even within an optimization loop.

Subsequent to the proof-of-concept study of 3D vane shaping to control shock interactions described previously, an optimized geometry of the downstream vane was discovered using a genetic algorithm. A downstream vane fitness function was derived based on how well the unsteadiness due to reflected shocks was concentrated in the root region of the upstream blade, as well as how widely the phase of remaining fluctuations was distributed over the span. This was in keeping with the characteristics achieved for the bowed vane, as described with reference to Fig. 3. The fitness of a particular vane f was defined as

$$f = \frac{(1 - S_{P'35})}{4} + \frac{\Delta\Phi}{3\pi} + \frac{1 - P'_{\text{loc}}}{2} \tag{1}$$

where $S_{P'35}$ is the fraction of the span at 95% axial chord where local pressure fluctuations fall to 35% of the maximum level for the HITRT vane and $\Delta\Phi$ is the peak-to-peak variation in the phase angle over the span at the same chordwise location. Again, it was argued in the Sec. II proof-of-concept studies that unsteadiness nearer to the root of the airfoil, where airfoil motion would be small in the event of a resonance, is less detrimental than unsteadiness occurring toward the tip. The quantity $(1 - S_{P'35})$ was included in the fitness function as a measure of the degree to which unsteadiness was driven toward the root of the airfoil as a consequence of airfoil bowing. Indeed, a fitness value of 1 for this difference term (before scaling) would indicate that unsteadiness had been driven off the airfoil surface entirely and onto the platform instead. Similarly, $\Delta\Phi$ was also stated to be potentially of value in reducing resonant stresses, although the net benefit would be entirely dependent on the mode shape in question. P'_{loc} is the amplitude of pressure fluctuations at 85% axial chord and 38% span as a fraction of the inlet total pressure. Initially, only the first two addends of Eq. (1) were used to evaluate vane fitness. However, as the optimization progressed, it was noted that significant unsteadiness due to cross-channel shock oscillations occurred outboard from the blade root, and this was attributed to the effect of the downstream vane pressure field as opposed to shock reflections. Accordingly, the third addend was included to address this additional source of unsteadiness.

It is worth noting that all three of these terms were selected only after a number of preliminary 3D unsteady CFD simulations with the specific HITRT blade–vane configuration before the optimization. After gaining a better understanding of the typical distribution of pressure fluctuations and the proper scaling for each of these terms, this fitness function was constructed. As will be shown Secs. V–VI, the proposed approximation by surface normal projections (ASNP) method does not require such prior knowledge of the airfoil configuration. Three-dimensional unsteady CFD simulations are required only for validation of the final solution after optimization has been performed.

With a fitness function in place, a very simple genetic algorithm was implemented in MATLAB® to allow for the exploration of the bowed-airfoil design space [32]. Vane airfoils were defined as five constant-radius cross-sections at even increments of fractional span, and these 2D profiles were unchanged throughout the design process; instead, the stacking of the cross-sections was varied through the optimization process. Each cross-section save the root was allowed to shift in the circumferential direction by up to 20% of the local pitch. No additional constraints were incorporated in the optimization. As we were performing a primarily aerodynamic study, our goal was to see what effects modification to the geometry might have on aerodynamic properties. In production, however, it is assumed that an engine designer would perform thorough analyses in all relevant areas (thermodynamics, structural integrity, etc.) before adopting a particular airfoil design.

The genome of each airfoil was defined by a 24-bit binary character string with 6 bits per allele. Genetic propagation was achieved by cutting the genomes at random locations and crossing them with mutation occurring at random in approximately two genes per generation via bit flipping. Latin hypercube sampling was used to create two island populations of 20 airfoils each, and the fitness of each airfoil was assessed according to Eq. (1). The top 24 individuals from the two populations were then mated to produce an initial population of 48 airfoils. Each generation was in turn culled to 24 mating individuals that were then randomly selected into mating pairs to produce two offspring per pair.

The process was repeated for 16 generations, and the airfoil with highest fitness was selected for manufacturing. The results of the optimization are given in Fig. 4 as a plot of fitness vs generation. Note that all three components of the fitness are plotted in the figure as well as the overall value. The fitness increased substantially over the process. The fitness of the baseline vane was 0.12 based on the application of Eq. (1), while that of the final bowed vane was 0.79, for an overall increase of 658%.

Downloaded by MASSACHUSETTS INST OF TECHNOLOGY (MIT - LINCOLN LAB) on July 9, 2014 | http://arc.aiaa.org | DOI: 10.2514/1.B35027

Downloaded by MASSACHUSETTS INST OF TECHNOLOGY (MIT - LINCOLN LAB) on July 9, 2014 | http://arc.aiaa.org | DOI: 10.2514/1.B35027

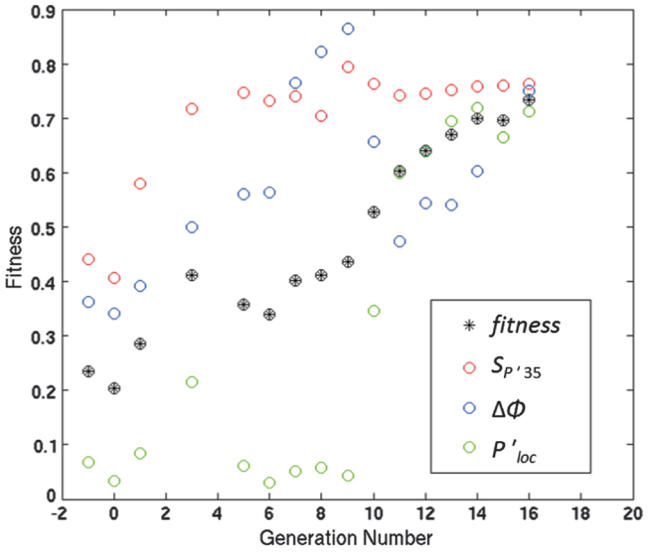

Fig. 4 Average vane fitness by generation for 3D unsteady optimization by genetic algorithm.

In total, 424 separate 3D unsteady RANS analyses were conducted using code LEO from Aerodynamic Solutions, Inc., [33] to find the final geometry of the downstream vane. This involved analyzing the steady-state flowfield for a full stage-and-one-half transonic turbine to convergence, calculating the periodic unsteady solution, and postprocessing the results over a pair of periodic intervals (see Sec. IV). In terms of wall-clock time, it was possible to complete this three-step analysis overnight on a dedicated cluster of 96 CPUs. The number of vanes evaluated in this design-optimization study was far in excess of what is typically used to define the aerodynamic shape of a state-of-the-art military engine in a large commercial engine company. A comparison between the blade suction-side unsteadiness due to the baseline and final, optimized vane geometries is shown in Fig. 5. It is clear that the optimization was successful in driving the unsteadiness due to reflected shocks to the root region of the blade (upper half of the figure) and distributing the phase of unsteadiness over the span in the region of interest (lower half of the figure). It is worth noting that, although the root of the blade was the preferred target for directed shocks in this case, it is clear that 3D airfoil shaping

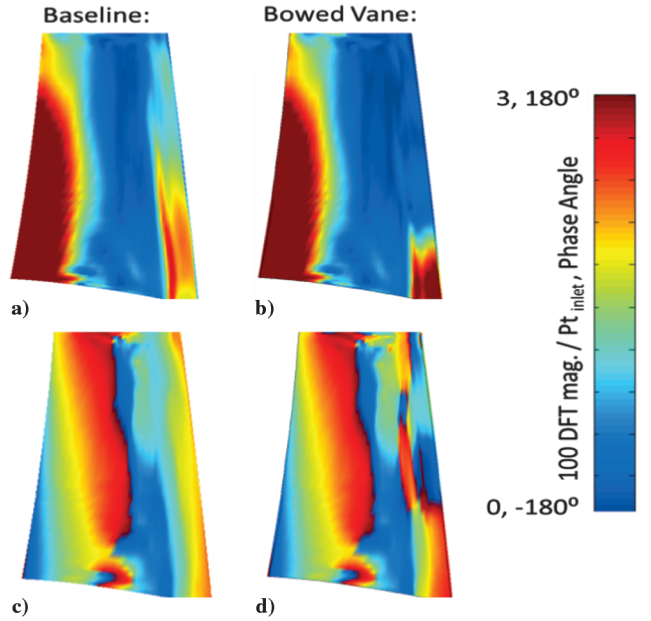

Fig. 5 The distribution of unsteady pressure in terms of DFT magnitude a)–b) and phase angle c)–d) on the blade suction side due to the baseline a) and c) and optimized b) and d) vanes.

can be used in general to tailor unsteady interactions (not just shock interactions but also viscous and potential field interactions) in both compressors and turbines. Also, 3D airfoil shaping may be used to mitigate secondary losses in turbines.

IV. Computational Methods

All design-optimization studies presented herein were undertaken with the 3D, multistage RANS code described by Ni et al. [33]. The code employs implicit dual time stepping to solve for the periodic-unsteady flowfield in a turbomachine on an OHHH-grid topology, and numerical closure is obtained via the k-ω turbulence model of Wilcox [34]. The code is accurate to second order in both space and time. The flow solver employs a finite-volume, cell-vertex Lax–Wendroff method, and both local time-stepping and multigrid techniques are used to obtain rapid convergence [35]. For time-accurate calculations of vane–blade interaction with the Ni code, the flowfield is solved on a portion of the annulus over which spatial periodicity occurs. This is not arduous in this instance since periodicity occurs on 1/23 of the annulus. That is, there are 23 inlet guide vanes, 46 rotating blades, and 23 downstream stationary vanes in the stage-and-one-half turbine.

Ooten [36] has done a comprehensive study of grid, time-step, and iterative convergence for the baseline geometry of the turbine and compared the predicted flowfield to that obtained experimentally in a short-duration facility by Clark and Grover [37]. He found excellent agreement between predictions and measurements of shock interactions for the baseline geometry, and lessons learned in that study are incorporated here. One upstream vane and one downstream vane passage were modeled in each simulation along with two blade passages. Airfoil passages were modeled with approximately 1.4 and 0.8 million grid points for stationary and rotating components, respectively, and the difference in counts is a consequence of preserving the circumferential grid spacing across sliding interfaces. In keeping with the investigation of Ooten [36], each final analysis employed 20 inner iterations and 200 global time steps per airfoil passing. By contrast, 10 inner iterations and 100 time steps per passing were used for all calculations during the unsteady optimization process. This simplification was necessary to enable the complete analysis of a new generation of the airfoil population overnight while still allowing the successful achievement of the objectives of the genetic algorithm. However, for all final comparisons carried out to assess the performance of any design outside the optimization routine, the lessons learned in the study of Ooten were followed, and the larger number of time steps and inner iterations were used.

V. Geometric Optimization of Bowed Vane

While it is evident from the previous results that 3D, unsteady optimization can lead to effective management of time-resolved flowfields, the computational time required to obtain a valid time-accurate CFD simulation is still considerable. In this case, the overall time required to achieve the optimum design was 16 days subsequent to the full coding of the system. So, following the success of the RANS-based design optimization discussed previously, an attempt was made to explore the space for airfoil bowing in a more time-effective manner. Since the success of vane bowing depends ultimately on a simple alteration of the local normal vector of the pressure surface, it was postulated that one might approximately assess the effects of 3D shaping on unsteadiness knowing only the geometries and locations of the airfoils. This allows for the analysis of an airfoil with respect to shock reflection within a few minutes by a single processor instead of the multiple hours and processors necessary in the case of a standard 3D unsteady simulation. Consequently, it is possible to explore the design space for airfoil bowing much more thoroughly with only a verification step requiring a full time-resolved analysis at the end of the process. This lack of dependence on time-resolved predictive tools and multistage models makes it possible to include the effects of shock wave propagation in relevant turbines at a much earlier stage in the design process.

Downloaded by MASSACHUSETTS INST OF TECHNOLOGY (MIT - LINCOLN LAB) on July 9, 2014 | http://arc.aiaa.org | DOI: 10.2514/1.B35027

A. Calculation of Magnitudes of Shock Reflections Using Surface Normals

As already mentioned, the direction of travel of the reflected shock will change if the local normal vector that stems from the point of contact on the downstream vane is modified. To calculate the effects of said geometric alterations, the vane pressure surface is treated as a patchwork of 3920 contiguous cells, 80 grid points streamwise (i direction) by 49 grid points spanwise (k direction). The position vector of each vertex is subtracted from the position vectors of adjacent vertices in both directions to produce two separate displacement vectors, the cross-product of which results in the normal vector of the cell (i, k):

$$\boldsymbol{d}_1 = (\boldsymbol{x}_{i,k}, \boldsymbol{y}_{i,k}, \boldsymbol{z}_{i,k}) - (\boldsymbol{x}_{i+1,k}, \boldsymbol{y}_{i+1,k}, \boldsymbol{z}_{i+1,k}) \tag{2}$$

$$\boldsymbol{d}_2 = (\boldsymbol{x}_{i,k}, \boldsymbol{y}_{i,k}, \boldsymbol{z}_{i,k}) - (\boldsymbol{x}_{i,k+1}, \boldsymbol{y}_{i,k+1}, \boldsymbol{z}_{i,k+1}) \tag{3}$$

$$\boldsymbol{n}_{i,k} = \boldsymbol{d}_1 \times \boldsymbol{d}_2 \tag{4}$$

The magnitude of this surface normal is proportional to the linear approximation of the surface area of the cell.

Once the outer normal direction from the vane pressure side is known, it is necessary to determine the intersection of the vector with the upstream, rotating blade row. Because the complex geometry of the upstream blade is incapable of being represented by a single equation, a standard algebraic approach for finding the intersection between a line and a plane is inadequate in this situation. Instead, a search is made to determine colinearity between the identified surface normal and all possible lines that can be made from vertices on the blade suction side to the origin of the surface normal on the vane. Although true colinearity is not typically found, the vertex on the blade that produces a slope nearest to that of the surface normal is taken as the vertex nearest to the location where a projection of that particular surface normal would impact the blade (see Fig. 6).

To avoid the inclusion of projections that approach the blade surface near its edge but do not intersect it, all normals that identify one of these border vertices as being closest to them are ignored. Because grid clustering techniques result in a greater concentration of vertices in regions of high local curvature [38], the vertices near the edges of the airfoils tend to have very small displacement vectors between them, and therefore relatively small cell normals. Thus, the loss of valid projections that are discounted despite having a nearest vertex located on the edge of the blade and landing within the boundaries of the blade are minimal. In the case of the HITRT blade used for the calculations in this paper, this discounted area accounts for less than 0.2% of the total surface area of the blade.

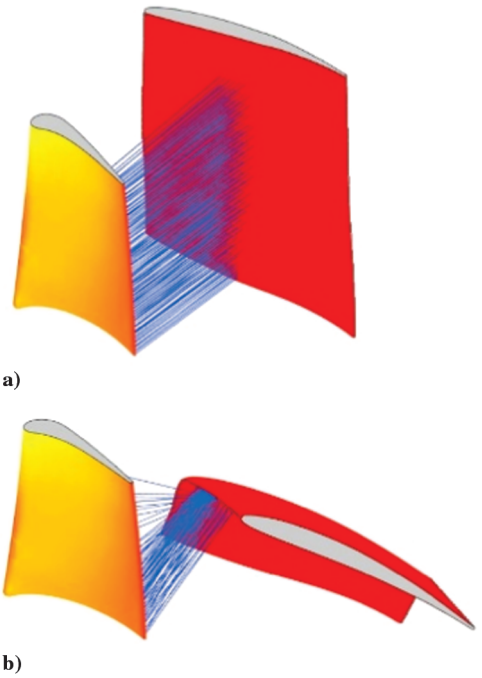

a)

b)

Fig. 6 Shock reflections projected to the blade from an a) normal and b) bowed HITRT vane.

a) b)

Fig. 7 The scaled magnitudes of shock reflections projected from an a) normal and b) bowed HITRT vane.

The purpose of determining where the surface normals from the downstream vane will intersect the surface of the upstream blade is to predict where the magnitude of pressure fluctuations (due to shock reflections) will be the greatest on the suction side of the blade. Because the cells used to calculate the surface normals vary widely in size, the magnitudes of their surface normals vary widely as well. Thus, instead of keeping track of a raw count of surface normals making contact at a particular location on the blade, we calculate the sum of the magnitudes of surface normals making contact at that point. We refer to this sum as the total reflection magnitude for that vertex. A greater total reflection magnitude indicates that a larger percentage of the vane pressure side surface will project shock waves to that location on the blade. Additionally, because the bowing of an airfoil increases its overall surface area, these total reflection magnitudes are scaled to equal a percentage of the total surface area of the projecting surface of the vane. Thus, regardless of the geometry of the downstream vane, the sum of scaled surface normal projections for any airfoil configuration is 1.

While the process described previously seems straightforward, there are additional factors that must be considered. First, although the magnitudes of these reflection totals do not have units of pressure directly, it is possible to plot them in order to illustrate the regions of the blade suction side that would see the largest scaled total reflection magnitudes of shock reflections produced by the surface normals from any given downstream vane geometry, as shown in Fig. 7. One can then use this information to identify trends, to make design decisions, and then to validate the benefit using a time-resolved simulation that gives more physical predictions of pressure magnitudes. Second, it is necessary to consider the line of sight available to surface normal vectors projected from the vane pressure side. The forward part of a vane in the wheel may intersect the normal projection coming from the aft of a neighboring vane, thereby preventing it from affecting the upstream rotating airfoil, as shown in Fig. 8. Finally, knowledge of the effects of shock waves within a flowfield gives further insight into the streamwise areas of the blade that are reachable by shock reflections. No reflected shocks can propagate further upstream than the cross-channel shock wave that travels from the pressure side of one blade to the suction side of the adjacent blade (see Fig. 1, location 1) since this location represents the choke plane of the stage. Therefore, any surface normals that project into that region of the airfoil are not included in the calculation.

B. Optimization by Genetic Algorithm

The very small computational requirements of the previous method coupled with the success already achieved with the demon-

Downloaded by MASSACHUSETTS INST OF TECHNOLOGY (MIT - LINCOLN LAB) on July 9, 2014 | http://arc.aiaa.org | DOI: 10.2514/1.B35027

Fig. 8 Blockage can occur when an adjacent vane is in the line of sight.

stration of full unsteady optimization suggested another attempt with a genetic algorithm (GA) to find the ideal bowed geometry. It also fostered a much more rigorous approach to the implementation of the genetic algorithm, and a wide variety of techniques was tried. The fitness function was based in part upon an equation borrowed from the field of rigid-body mechanics. Analogous to determining the center of gravity of an object, the equation used to find the center of reflection is given by

$$C_r = \frac{\sum r_i m_i}{\sum m_i} \tag{5}$$

In this case, C_r represents the center of reflection, r_i is the radial distance of the vertex i from the root, and m_i is the magnitude of the reflections at that vertex. This calculation returns the average spanwise location of the reflections, with a lower value representing a center of reflection closer to the root of the blade. The second criterion employed was the sum of the magnitudes of all normal projections contacting the blade, with a lower sum being preferred. Each individual was given a total fitness score between 0 and 1, which combined these two factors, thereby driving the reflections to the root of the blade without unnecessarily increasing the overall magnitude of shock expected to make contact with the blade.

Ultimately, the fitness f of individuals in the population was represented by the equation

$$f = (0.5)C_r + (0.5)\frac{\Sigma m_{i'} - \Sigma m_i}{\Sigma m_{i'}} \tag{6}$$

where $\Sigma m_{i'}$ is equal to the total scaled reflection magnitude of the baseline geometry. This formulation weighted equally a reduction in the total scaled reflection magnitude and a redirection of the surface normals to a span location closer to the root of the blade. For the HITRT geometry, $\Sigma m_{i'} = 0.16$. For the vast majority of designs, $\Sigma m_i \leq \Sigma m_{i'}$, since the optimization algorithm was intended to reduce the total reflection magnitude. In rare cases in which the total reflection magnitude has actually increased, the second term of Eq. (6) may have a small negative value, but the overall fitness value will almost certainly remain within the bounds of 0 and 1.

Individuals were represented by 48-bit character strings, with each 12 bits converting to a decimal number between a user-defined minimum and maximum pitch change percentage (typically $-1.0 \leq \min \leq 0 \leq \max \leq 1.0$) that varied between numerical experiments as various parameter combinations were tried. Using the HITRT downstream vane as a baseline geometry, individuals were created for analysis by bowing in the manner described in Sec. II, using the four pitch factors to determine the circumferential shift of the cross-sections at predetermined radii equal to the 25, 50, 75, and 100% span. The majority of optimization routines were run with a maximum pitch change per cross-section of 20% of the local pitch, thus matching the constraints that were used for the CFD optimization routine. To maintain the speed of the ASNP routine, no additional constraints (such as maximum allowable stresses in various points of the airfoil) were included in the optimization. This method is meant to be used in conjunction with more sophisticated and computationally intense software for confirmation of feasibility in the final design.

To avoid premature convergence, large population sizes were used (typically $\mu = 80$), and a linear ranking selection was used with a value of selective pressure equal to 1.25 (i.e., meaning the expected number of offspring allotted to the fittest individual was 1.25). The equation used for determining selective probability was given by

$$P_k = \frac{(2-s)}{\mu} + \frac{2k(s-1)}{\mu(\mu-1)} \tag{7}$$

where P_k is the probability of member k being selected to mate if the individuals are ranked from 1 to k in ascending order of fitness and μ is the population size. In this case, a stochastic universal sampling approach was taken rather than a simple roulette-wheel algorithm in order to decrease discrepancies between selective probabilities and actual survival rates. Also, an elitist function was included to guarantee the inclusion of the four fittest individuals in each generation in the following generation of parents. Binary gray coding was selected rather than natural binary coding to allow for a uniform Hamming distance of 1 between adjacent values, meaning that each expressible number differed from the nearest expressible number on either side by only 1 bit (see Table 1). This gave the mutation function more flexibility in terms of local searching for a relative maximum [39].

In every iteration of the optimization process, the stochastic nature of genetic algorithms guaranteed a different population. Furthermore, a slight change in any of the GA parameters (such as the encoding method, mutation rate, or number of bits per allele) could have a significant effect on the variance of the population, number of generations required for convergence, discovery of absolute maxima/minima over local ones, etc. Shown in Fig. 9, however, are the trends that were seen repeatedly in the GA implementations that were attempted.

As shown by the graphs, rapid improvement in fitness was seen during approximately the first 15 generations as more obviously undesirable traits were culled from the population. The generations that followed continued to make minor increases in fitness, center of reflection, and reflection magnitudes, but with diminishing returns over time.

C. Validation of ASNP Method Through Computational Fluid Dynamics Analyses

After running the GA based on the ASNP method, the 27 individuals demonstrating unique characteristics of unsteady pressure distribution and the highest fitness scores were then analyzed

Table 1 With gray coding, the Hamming distance between adjacent integers is always 1, often allowing for smaller mutation steps caused by one bit switch while not significantly limiting the maximum step size

Base 10 (n)	Natural binary	Hamming distance from $n-1$	Position(s) of switches
5	0101	— —	— —
6	0110	2	3, 4
7	0111	1	4
8	1000	4	1, 2, 3, 4
Base 10 (n)	Gray binary	Hamming distance from $n-1$	Position(s) of switches
5	0111	—	—
6	0101	1	3
7	0100	1	4
8	0110	1	3

Downloaded by MASSACHUSETTS INST OF TECHNOLOGY (MIT - LINCOLN LAB) on July 9, 2014 | http://arc.aiaa.org | DOI: 10.2514/1.B35027

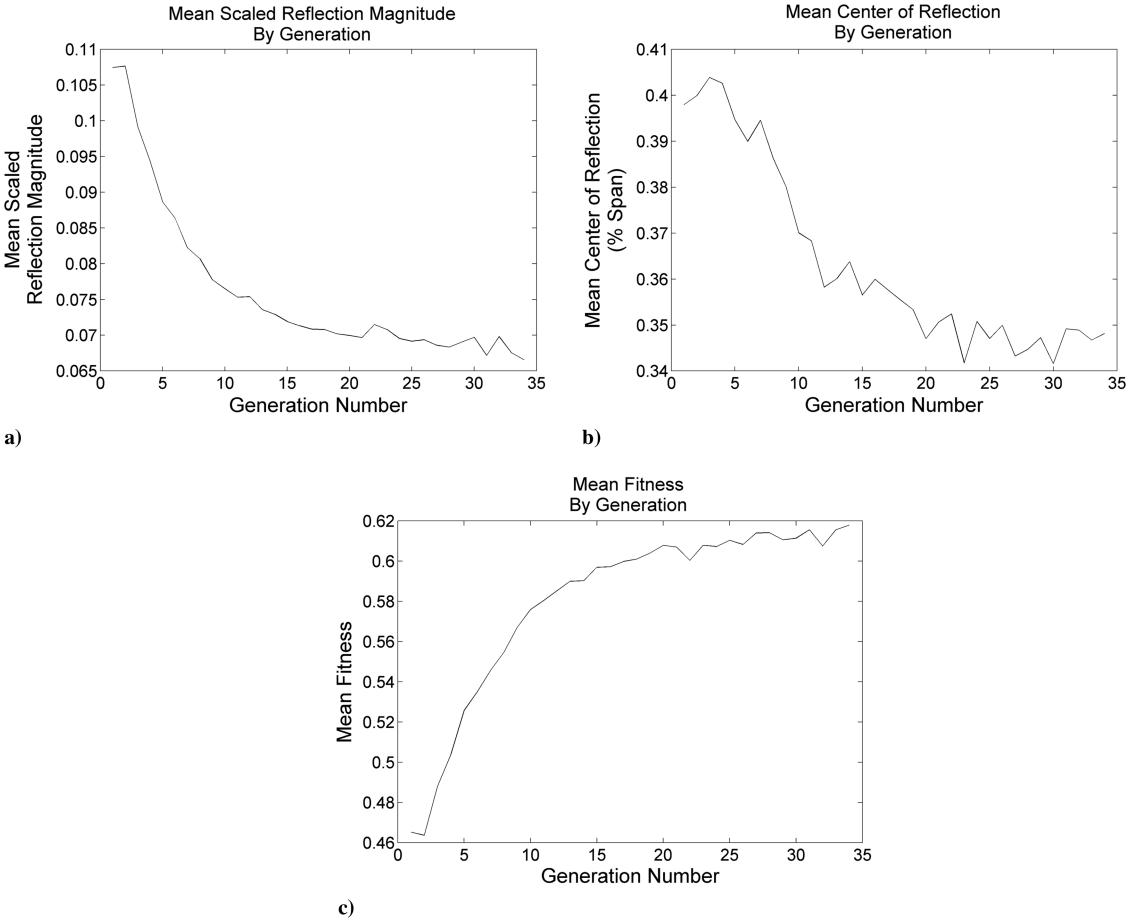

Fig. 9 Genetic algorithms results for a) mean scaled reflection magnitude, b) mean center of reflection, and c) total fitness.

using the same time-resolved simulations employed for the demonstration of full 3D unsteady optimization. The results confirmed not only that the ASNP method produced many individuals that more thoroughly directed shock reflections to the root of the blade but also that it could accomplish the task far more quickly. It was possible to analyze as many as 80 individuals by 45 generations in the same amount of wall-clock time as one full 3D unsteady optimization, an improvement in analysis time per airfoil by over four orders of magnitude. Shown in Figs. 10c and 10d are the pressure distributions of two of the high fitness individuals created by a run of the ASNP GA, given 80 individuals and 18 generations total. These pressure distributions equate to less than 1% of the unsteadiness caused by shock reflections, which is produced by the baseline vane.

The corresponding 3D geometries of the bowed vanes that resulted in these pressure distributions are shown in Fig. 11. The baseline vane shows a very typical profile for a vane used in a setting such as the HITRT. The full unsteady RANS optimal design shows a tendency to bow more as the span increases. The first of the two ASNP optimal designs seems to favor bowing closer to its root. The fourth design is one generated when the optimization constraint for the maximum allowable bowing per cross-section was loosened from 20% of the local pitch to 50%. While the geometry appears to be significantly different than the baseline vane, it is interesting to note that a very desirable pressure distribution was nonetheless achievable with these larger allowable pitch changes. Table 2 gives the exact bowing pitch percentages for each of the four vanes.

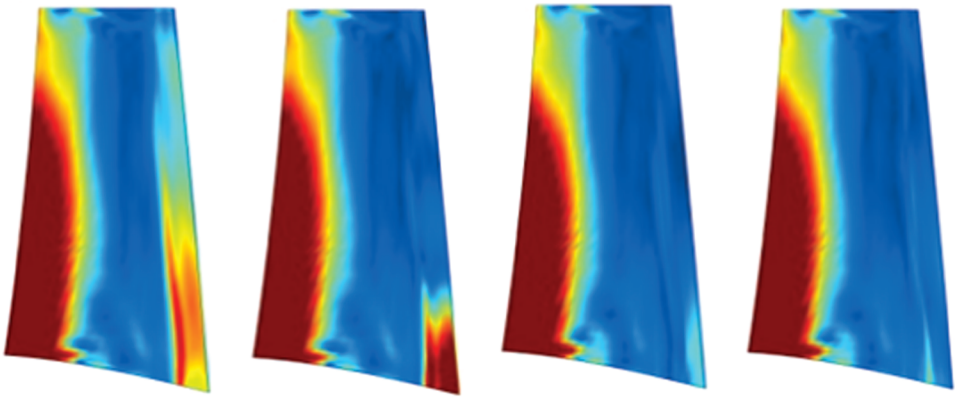

Fig. 10 DFT magnitudes due to the a) baseline, b) RANS optimal, and c)–d) ASNP genetic algorithm vanes.

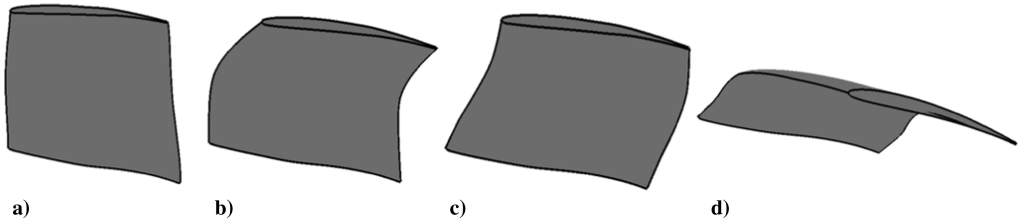

a) b) c) d)

Fig. 11 The 3D geometries of the a) baseline, b) RANS optimal, and c)–d) ASNP genetic algorithm vanes.

Table 2 The percent of local pitch that each downstream vane shifted in the circumferential direction at the given span locations

Vane	0% span	25% span	50% span	75% span	100% span
Baseline	0	0	0	0	0
RANS optimal	0	1	7	17	20
ASNP optimal 1	0	18	18	10	1
ASNP optimal 2	0	30	23	49	40

VI. Conclusions

The importance of developing design methodologies for the prediction and control of time-varying pressure fields in transonic turbines cannot be overstated. The concept of vane bowing for the redirection of reflected shock waves was explored with proof-of-concept numerical experiments and a full 3D unsteady optimization. Furthermore, a new method for predicting these shock reflections was proposed and evaluated. The ASNP method was shown to require only the airfoil geometries and locations as input, obviating the need to perform a full time-resolved analysis, and the advantages of this flexibility were identified. The calculations performed to compute the shock reflections were given, and an explanation of which regions of the blade were subjected to the effects of these reflections was included. The fitness function and operating parameters of a genetic algorithm intended to produce low shock-reflection magnitudes on the upstream blade and drive existing reflections to the root of the blade were discussed. High-fitness individuals produced by the ASNP method were validated by full 3D unsteady RANS analysis, showing an overall improvement in reducing pressure fluctuations due to shock interactions by two orders of magnitude, with a turnaround time per airfoil smaller than that of CFD optimization by four orders of magnitude. The proposed ASNP method can be used early in the 3D aerodesign process to estimate the forcing function experienced by the HPT blade with significant advantages over an approach consisting exclusively of time-resolved, multirow simulations.

Acknowledgments

The advice and support of Bob Ni of Aerodynamic Solutions, Inc., and Frank Huber and Dean Johnson of Florida Turbine Technologies, Inc., during the course of this study is gratefully acknowledged. Also, thanks are due to Peter Koch and Michael Ooten of U.S. Air Force Research Laboratory for their aerodynamic design work on the baseline High-Impact Technologies Research Turbine geometry.

References

[1] Tyler, J. M., and Sofrin, T. G., "Axial Flow Compressor Noise Studies," *Society of Automotive Engineers Transactions*, Vol. 70, No. 1, 1970, pp. 309–332.

[2] Rangwalla, A. A., and Rai, M. M., "A Numerical Analysis of Tonal Acoustics in Rotor-Stator Interactions," *Journal of Fluids and Structures*, Vol. 7, No. 6, 1993, pp. 611–637. doi:10.1006/jfls.1993.1037

[3] Dring, R. P., Joslyn, H. D., Hardin, L. W., and Wagner, J. H., "Turbine Rotor-Stator Interaction," *Journal of Engineering for Power*, Vol. 104, No. 4, 1982, pp. 729–742. doi:10.1115/1.3227339

[4] Dunn, M. G., and Haldeman, C. W. Jr., "Phase-Resolved Surface Pressure and Heat-Transfer Measurements on the Blade of a Two-Stage Turbine," *Journal of Fluids Engineering*, Vol. 117, No. 4, 1995, pp. 653–658. doi:10.1115/1.2817318

[5] Rai, M. M., "Navier–Stokes Simulations of Rotor-Stator Interaction Using Patched and Overlaid Grids," *Journal of Propulsion and Power*, Vol. 3, No. 5, 1987, pp. 387–396. doi:10.2514/3.23003

[6] Giles, M. B., "Stator/Rotor Interaction in a Transonic Turbine," *Journal of Propulsion and Power*, Vol. 6, No. 5, 1990, pp. 621–627. doi:10.2514/3.23263

[7] Paniagua, G., and Denos, R., "Unsteadiness in HP Turbines," *Advances in Turbomachinery Aero-Thermo-Mechanical Design Analysis*, von Kármán Inst. Lecture Series 2007–02, von Kármán Inst. for Fluid Dynamics, Sint-Genesius-Rode, Belgium, 2007, pp. 37–44.

[8] Greitzer, E. M., Tan, C. S., Wisler, D. C., Adamczyk, J. J., and Strazisar, A. J., "Unsteady Flows in Turbomachines: Where's the Beef?," *Unsteady Flows in Aeropropulsion*, edited by Ng, W., Fant, D., and Povinelli, L., AD-Vol. 40, ASME, New York, 1994, pp. 1–11.

[9] Sharma, O. P., Pickett, G. F., and Ni, R. H., "Assessment of Unsteady Flows in Turbines," *Journal of Turbomachinery*, Vol. 114, No. 1, 1992, pp. 79–90. doi:10.1115/1.2928001

[10] Hilbert, G. R., Ni, R. H., and Takahashi, R. K., "Forced-Response Prediction of Gas Turbine Rotor Blades," *Analysis and Design Issues for Modern Aerospace Vehicles, Proceedings of ASME International Mechanical Engineering Congress and Exposition*, American Society of Mechanical Engineers, New York, Nov. 1997, pp. 491–498.

[11] Green, J. S., and Marshall, J. G., "Forced Response Prediction within the Design Cycle," *IMechE Conference Transactions 1999-1A*, Inst. of Mechanical Engineers, London, pp. 377–391.

[12] Chiang, H. D., and Kielb, R. E., "An Analysis System for Blade Forced Response," *Journal of Turbomachinery*, Vol. 115, No. 4, 1993, pp. 762–770. doi:10.1115/1.2929314

[13] Seinturier, E., Lombard, J.-P., Dumas, M., Dupont, C., Sharma, V., and Dupeux, J., "Forced-Response Methodology for the Design of HP Compressors Bladed Disks," American Soc. of Mechanical Engineers Paper GT2004-53372, New York, 2004.

[14] Montgomery, M., Tartibi, M., Eulitz, F., and Schmitt, S., "Application of Unsteady Aerodynamics and Aeroelasticity in Heavy Duty Gas Turbines," American Soc. of Mechanical Engineers Paper GT2005-68813, New York, 2005.

[15] Filsinger, D., Frank, Ch., and Schafer, O., "Practical Use of Unsteady CFD and FEM Forced Response Calculation in the Design of Axial Turbocharger Turbines," American Soc. of Mechanical Engineers Paper GT2005-68439, New York, 2005.

[16] Sipatov, A. M., Gladisheva, N. V., Avgustinovich, V. G., and Povishev, I. A., "Tools for Estimating Resonant Stresses in Turbine Blades," American Soc. of Mechanical Engineers Paper GT2007-27196, New York, 2007.

[17] Anderson, A. D., Jr., *Modern Compressible Flow with Historical Perspective*, McGraw–Hill, New York, 1982, pp. 74–77.

[18] Joly, M., Verstraete, T., and Paniagua, G., "Attenuation of Vane Distortion in a Transonic Turbine Using Optimization Strategies, Part I—Methodology," American Soc. of Mechanical Engineers Paper GT2010-22370, New York, 2010.

[19] Joly, M., Paniagua, G., and Verstraete, T., "Attenuation of Vane Distortion in a Transonic Turbine Using Optimization Strategies, Part II—Optimization," American Soc. of Mechanical Engineers Paper GT2010-22371, New York, 2010.

[20] Clark, J. P., Aggarwala, A. S., Velonis, M. A., Magge, S. S., and Price, F. R., "Using CFD to Reduce Resonant Stresses on a Single-Stage, High-Pressure Turbine Blade," American Soc. of Mechanical Engineers Paper GT2002-30320, New York, 2002.

[21] Dunn, M. G., "Convective Heat Transfer and Aerodynamics in Axial Flow Turbines," *Journal of Turbomachinery*, Vol. 123, No. 4, 2001,

Downloaded by MASSACHUSETTS INST OF TECHNOLOGY (MIT - LINCOLN LAB) on July 9, 2014 | http://arc.aiaa.org | DOI: 10.2514/1.B35027

pp. 637–686.
doi:10.1115/1.1397776
[22] Adamczyk, J. J., "Aerodynamic Analysis of Multi-Stage Turbomachinery Flows in Support of Aerodynamic Design," *Journal of Turbomachinery*, Vol. 122, No. 2, 2000, pp. 189–217.
doi:10.1115/1.555439
[23] Rao, K. V., Delaney, R. A., and Dunn, M. G., "Vane-Blade Interaction in a Transonic Turbine, Part 1: Aerodynamics," *Journal of Propulsion and Power*, Vol. 10, No. 3, 1994, pp. 305–311.
doi:10.2514/3.23757
[24] Busby, J. A., Davis, R. L., Dorney, D. J., Dunn, M. G., Haldeman, C. W., Jr., Abhari, R. S., Venable, B. L., and Delaney, R. A., "Influence of Vane-Blade Spacing on Transonic Turbine Stage Aerodynamics, Part II: Time-Resolved Data and Analysis," American Soc. of Mechanical Engineers Paper 1998-GT-482, New York, 1998.
[25] Hilditch, M. A., Smith, G. C., and Singh, U. K., "Unsteady Flow in a Single Stage Turbine," American Soc. of Mechanical Engineers Paper 1998-GT-531, New York, 1998.
[26] Haldeman, C. W., Dunn, M. G., Abhari, R. S., Johnson, P. D., and Montesdeoca, X. A., "Experimental and Computational Investigation of the Time-Averaged and Time-Resolved Pressure Loading on a Vaneless Counter-Rotating Turbine," American Soc. of Mechanical Engineers Paper 2000-GT-0445, New York, 2000.
[27] Kost, F., Hummel, F., and Tiedemann, M., "Investigation of the Unsteady Rotor Flow in a Single-Stage HP Turbine Stage," American Soc. of Mechanical Engineers Paper 2000-GT-0432.45, New York, 2000.
[28] Laumert, B., Martensson, H, and Fransson, T. H., "Investigation of Unsteady Aerodynamic Blade Excitation Mechanisms in a Transonic Turbine Stages," American Soc. of Mechanical Engineers Paper GT2002-30450, New York, 2002.
[29] Bakhle, M. A., Liu, J. S., Panovsky, J., Keith, T. G., and Mehmed, O., "Calculation and Correlation of the Unsteady Flowfield in a High Pressure Turbine," American Soc. of Mechanical Engineers Paper GT2002-30322, New York, 2002.
[30] Jennions, I. K., and Adamczyk, J. J., "Evaluation of the Interaction Losses in a Transonic Turbine HP Rotor/LP Vane Configuration," *Journal of Turbomachinery*, Vol. 119, No. 1, 1997, pp. 68–75.
doi:10.1115/1.2841012
[31] Ni, R. H., "Advanced Modeling Techniques for New Commercial Engines," *XIV ISABE Conference*, International Society for Air Breathing Engines, Cincinnati, OH, Sept. 1999.
[32] Manzi, J., "The Origin of Species and Everything Else—Coping with Evolution and Religion," *National Review*, Vol. LXI, No. 18, 2007, pp. 42–46.
[33] Ni, R. H., Humber, W., Fan, G., Johnson, P. D., Downs, J., Clark, J. P., and Koch, P. J., "Conjugate Heat Transfer Analysis of a Film-Cooled Turbine Vane," American Soc. of Mechanical Engineers Paper GT2011-45920, New York, 2011.
[34] Wilcox, D. C., *Turbulence Modeling for CFD*, 2nd ed., DCW Industries, Inc., La Cañada, CA, 2003, pp. 136–140.
[35] Lax, P. D., and Wendroff, B., "Difference Schemes for Hyperbolic Equations with High Order Accuracy," *Communications on Pure and Applied Mechanics*, Vol. 17, No. 4, 1964, pp. 381–398.
doi:10.1002/cpa.3160170311
[36] Ooten, M. K., "Unsteady Aerodynamic Interaction in a Closely-Coupled, Contra-Rotating," M.S. Thesis, University of Dayton, Dayton, OH, 2013.
[37] Clark, J. P., and Grover, E. A., "Assessing Convergence in Predictions of Periodic-Unsteady Flowfields," *Journal of Turbomachinery*, Vol. 129, No. 4, 2007, pp. 740–749.
doi:10.1115/1.2720504
[38] Thompson, J. F., Soni, B. K., and Weatherill, N. P., *Handbook of Grid Generation*, CRC Press, Boca Raton, FL, 1999, pp. 210–232.
[39] Eiben, A. E., *Introduction to Evolutionary Computing*, Springer–Verlag, New York, 2003, pp. 45–46.

F. Liu
Associate Editor

Downloaded by MASSACHUSETTS INST OF TECHNOLOGY (MIT - LINCOLN LAB) on July 9, 2014 | http://arc.aiaa.org | DOI: 10.2514/1.B35027